

## The Impact of Spatial Resolution Enhancement of SSM/I Microwave Brightness Temperatures on Rainfall Retrieval Algorithms

MICHAEL R. FARRAR,\* ERIC A. SMITH, AND XUWU XIANG

*Department of Meteorology, and Supercomputer Computations Research Institute, The Florida State University, Tallahassee, Florida*

(Manuscript received 9 October 1992, in final form 19 April 1993)

### ABSTRACT

The impact of spatial resolution enhancement on estimates of tropical typhoon rainfall based on SSM/I (Special Sensor Microwave/Imager) measurements is evaluated with six different microwave precipitation retrieval algorithms. Passive microwave estimates of rainfall are susceptible to errors from nonhomogeneous beam filling. The SSM/I ground footprints for the 19-, 22-, and 37-GHz channels have considerable overlap, and thus deconvolution techniques can be applied to enhance spatial resolution of measurements at those frequencies. The authors utilize a Backus–Gilbert matrix transform approach to accomplish the deconvolution so as to minimize noise amplification, as suggested by Stogryn. The deconvolution scheme is evaluated in terms of its impact on rain rates throughout the life cycles of seven tropical cyclones that occurred during the 1987 hurricane and typhoon season. The evaluation was performed on a single-frequency emission-based algorithm, a single-frequency scattering-based algorithm, two multiple-frequency statistical regression algorithms, and two physical inversion-based profile algorithms. While rainfall patterns detected by all algorithms were qualitatively enhanced by accentuating rainfall gradients and other smaller-scale features, quantitative responses to the deconvolution process were quite different for each algorithm. Furthermore, each of the algorithms, which uses its own distinct scientific approach, exhibits its own distinct properties in retrieving the rainfall patterns and in recovering the storm domain-averaged rain rates. The rain rates derived from the single-frequency emission algorithm were consistently increased by application of the deconvolution procedure. Time- and space-averaged rain rates were elevated by approximately 5%–6% due to the nonlinear relationship of rain rate to brightness temperature. On the other hand, rain rates from the single-frequency scattering algorithm were consistently reduced, with the time-space-averaged reduction between 10% and 20%. This effect is not algorithm related but is due to alteration of noise properties of the two polarized 37-GHz channels introduced during the deconvolution process. The multiple-frequency algorithms have more complex responses to deconvolution. Although instantaneous rain rates can be changed quite significantly by these methods, differences between deconvolved and raw time-space-averaged rain rates are small compared to the single-channel algorithms because the pixel-scale differences tend to be of a more random nature (positive and negative changes instead of consistent bias). However, it appears that the profile methods can undergo the greatest improvement to instantaneous rain rates after deconvolution is applied because they use perturbative inversion procedures rather than fixed brightness temperature–rain rate relationships.

### 1. Introduction

Due to the potential for hurricanes to cause destruction by flooding and high winds, the observation and prediction of tropical storms and cyclones has long been given high priority. Measurement of rainfall within these storms is also important for both observational and forecasting purposes. Rodgers and Adler (1981) utilized *Nimbus-5* Electrically Scanning Microwave Radiometer (ESMR) data to study the precipitation characteristics of several Pacific tropical cyclones. They found that storm intensification was well

correlated with increase in total storm rainfall, as estimated from the satellite measurements. They also noted that intensifying storms exhibited an increase in the relative contribution by the heavier rain areas to the total storm rainfall (rain rates greater than  $5 \text{ mm h}^{-1}$ ) and that the rainbands associated with the maximum rain rates had a smaller radius for intensified storms.

Measurements of rainfall can also be useful in predicting storm dissipation. Lewis and Jorgensen (1978) utilized radar data to measure rainfall from Hurricane Gertrude and showed that precipitation intensity decreased rapidly as the storm dissipated. Area-integrated rainfall decreased fourfold during a 6-h period when the storm was undergoing rapid dissipation. Hence, satellite-derived precipitation estimates can provide valuable information for intensity forecasting of tropical storms. Due to the lack of radar information away from coastlines and the expense of aircraft penetrations,

\* Current affiliation: Satellite Processing, Air Force Global Weather Central, Offutt Air Force Base, Nebraska.

Corresponding author address: Eric A. Smith, Department of Meteorology, The Florida State University, Tallahassee, FL 32306-3034.

satellite remote sensing is now considered by many to be the best alternative for estimating rainfall within hurricane-force storms.

Due to the inability of visible and infrared radiation to penetrate the cloud and directly sense precipitation particles, measurements in the microwave regime have been utilized by a number of researchers to address the rainfall retrieval problem. Wilheit et al. (1977) first demonstrated how 19-GHz measurements from the *Nimbus-5* ESMR could be used in a physical emission-type algorithm to retrieve precipitation rates over the ocean. Since that time many statistical and physical algorithms have been developed and tested. Spencer (1986) employed bipolarized 37-GHz measurements from the *Nimbus-7* Scanning Multichannel Microwave Radiometer (SMMR) in an algorithm that used a storm's scattering signature to estimate oceanic rain rates. Smith and Mugnai (1988) developed a set of single-frequency physically based algorithms that were based on a cloud model simulation for establishing the brightness temperature-rain rate relationships. Spencer et al. (1989) advanced the scattering approach based on a polarized corrected temperature (PCT) scheme for applications with Special Sensor Microwave/Imager (SSM/I) measurements; see CalVal (1989) for background information on the SSM/I instrument. The PCT transformation converts low temperature but highly polarized ocean scenes (low-emissivity signatures) to high PCT values while converting low temperature but mostly unpolarized deep convection scenes (large ice particle-water drop scattering signatures) to low values. Olson (1989) developed a multifrequency (four bipolarized channels at 10.7, 18, 21, and 37 GHz) inversion-type algorithm based on hypothetical microphysical structures to estimate precipitation in hurricanes while situated over water. Kummerow et al. (1989) and Kummerow et al. (1991) have explored an inversion-type algorithm that generates the complete rain-rate profile, based on a set of microphysical structures gleaned from aircraft radar data. Wilheit et al. (1991) utilized the Wilheit et al. (1977) radiation model (RTE) to devise an area-time-averaged inversion-type algorithm that iteratively adjusts an idealized lognormal rain-rate distribution in the forward RTE model until a modeled brightness temperature histogram at 19 GHz is in conformation with the measured histogram. This advanced a simpler area-time-average scheme of Shin et al. (1990) that used the same radiation model to aid in removing the non-raining background component (assumed to be normally distributed) from a measured brightness temperature histogram, leaving the raining component as the residual. Smith et al. (1992a), Smith et al. (1992b), Smith et al. (1994), Mugnai et al. (1993), and Xiang et al. (1992) have extended the profile method in a physical inversion-type algorithm, using a three-dimensional nonhydrostatic cloud model to define initial-guess information, for retrieving vertical profiles of four

classes of hydrometeor constituents (suspended cloud droplet and ice particles along with precipitating rain and ice particles). Hinton et al. (1992) have devised a method to combine a group of single-channel brightness temperature-rain rate relationships into a multi-channel algorithm, using a hybrid physical-statistical approach to obtain the retrievals. Adler et al. (1993) have combined physically based microwave retrievals with rain estimates from geosynchronous infrared data based on the Arkin and Meisner (1987) convective index (GPI) to bring the IR estimates into statistical conformation with the microwave estimates. This algorithm takes advantage of both the greater time-space sampling of the geosynchronous measurements and the greater fidelity of the microwave measurements (insofar as sensitivity to rainfall) to produce global datasets.

A fundamental problem that has impacted the results of all of these studies to varying degrees is the limited spatial resolutions (large ground footprints) of the passive microwave measurements themselves. Because the spatial scales of precipitation bands are often well below the spatial scales of the microwave ground footprints, incomplete beam filling or nonhomogeneous beam filling will generally lead to errors in the precipitation estimates to the degree that the brightness temperature-rain rate relationships inherent to the algorithms are nonlinear. This was first noted by Smith and Kidder (1978).

The main focus of this study is to determine the sensitivity of various of the above precipitation algorithms to inhomogeneous beam filling in passive microwave measurements of tropical cyclones. We have utilized measurements from the latest space-borne passive microwave radiometer, the four-frequency SSM/I, to obtain instantaneous rain rates. Some design improvements were made to SSM/I (Hollinger et al. 1990), which has greater ground coverage (approximately 80% increase in swath width) and less instrumental noise than its *Nimbus* predecessors (ESMR 5, ESMR 6, SMMR). However, the problem of large ground footprints remains. For reasons explained in the next section, each channel frequency has an increasingly larger ground footprint dimension as the frequency is reduced, such that each effectively samples a different spatial scale. As addressed by Mugnai et al. (1990), such mismatches in radiometer fields of view generally lead to nonlinear complications in the radiative transfer models utilized to determine rain rates from microwave brightness temperatures. Smith and Kidder (1978) compared radar-derived rain rates [obtained from shipboard measurements taken during the GARP (Global Atmospheric Research Program) Atlantic Tropical Experiment (GATE)] with rain rates derived from satellite measurements made by the *Nimbus-5* ESMR. They determined that the nonlinear relationship between rain rate and brightness temperature caused a mean underestimation in rain rate of approximately  $2 \text{ mm h}^{-1}$  for all the ESMR measure-

ments used in the study. In a more recent study, Short and North (1990) found that incomplete beam filling in the ESMR 5 measurements resulted in a 50% underestimation of rainfall when compared to radar-derived values. This problem has also been studied by Chiu et al. (1990). For these reasons, we introduce a spatial deconvolution technique (Farrar and Smith 1992), which, by taking advantage of footprint overlap in the lower frequencies, seeks to match the differing fields of view (FOV) of the SSM/I channels before using the measurements in the retrieval of rainfall. In the process, the resolutions of the lower-frequency channels are spatially enhanced to within proximity of the resolution of the highest-frequency channel. As this study is being conducted for tropical cyclones, which generally contain precipitation bands of greater areal coverage and homogeneity than the ensemble of cloud systems studied by Short and North (1990), the beam-filling effects are expected to be less pronounced.

Through the introduction of spatially enhanced measurements, we are not only attempting to improve the rainfall retrievals but also the rainfall imagery itself. Since the deconvolution method increases the spatial resolution, boundaries between precipitating and non-precipitating regions, which become smoothed by the large instrument fields of view, are better revealed. The enhancement of small-scale features leads to improvements in the mapping of the precipitation locations within the storms (e.g., eyewall depiction), which can be useful for tropical storm monitoring and forecasting, as well as for scientific investigations concerned with microphysical storm structure.

## 2. Nature of problem

Due to the very low levels of energy in the microwave spectrum passively emanating from the earth-atmosphere system, it has always been required that space-orbiting instruments measure the radiation over large FOVs or large "effective" apertures. This is necessary to ensure an adequately high signal-to-noise ratio but results in quite large ground footprints, relative to the scales of meteorological phenomena under study. Moreover, because of the diffraction limit characteristics associated with antenna systems on passive microwave radiometers for far-field conditions, the Fresnel region approximation dictates that as frequency decreases the FOV pattern increases for a given gain threshold (3 dB on SSM/I). That is why multifrequency radiometers produce collocated but dissimilar FOVs. For SSM/I, which is a conical scanner and thus preserves the ground footprint dimensions at a given frequency, the downtrack-crosstrack dimensions (km) are approximately  $69 \times 43$ ,  $60 \times 40$ ,  $37 \times 29$ , and  $15 \times 13$  for the 19-, 22-, 37-, and 85-GHz channels, respectively.

When utilizing measurements at different frequencies in multichannel retrieval algorithms or other

quantitative modeling applications, it is often desirable that the measurements be exactly matched in time and space. Identical antenna boresights for each respective satellite channel (or identical central points of the ground footprints) do not guarantee spatial conformation, that is, the lower-frequency channels with the larger FOVs sample larger surface areas. As a result, a specific SSM/I 19-GHz channel may sample a small but significant feature such as a thunderstorm, which may lie outside of the collocated FOV of the 85-GHz channel. Hence, comparisons of measurements at multiple frequencies are hampered by the fact that different phenomena are being sampled by different channels, and thus, FOV content is not preserved across the measurement set. That is basically why uniform spatial resolution is generally desirable for multichannel applications, as opposed to the lesser problem of detail blending within a given FOV.

This requirement poses a dilemma. One must either average the high-resolution measurements down to the scale of the lowest-resolution channel or, alternatively, attempt to improve or enhance the low-resolution measurements up to that of the highest-resolution channel. As the former results in the loss of smaller-scale feature information, the latter is obviously preferred. The optimal methods for increasing spatial resolution rely on an overlap of the gain functions of adjacent antenna temperature measurements. This redundancy of information makes it possible to retrieve information, namely, deconvolved brightness temperatures, on scales smaller than those directly sensed by the antenna.

## 3. Spatial deconvolution by Stogryn's method

Various methods have been employed by investigators to describe brightness temperatures of specified regions in terms of measured antenna temperatures. Claassen and Fung (1974) proposed a matrix inverse technique that concentrated on the cross-polarization effects of the measuring instrument and approximated the measured brightness temperature distributions by spherical bands. The solution coefficients were then determined by integrations of the antenna gain over the spherical bands. An alternative method was developed by Holmes et al. (1975), which was based on Fourier transforms. However, these methods have the undesirable side effect of amplifying noise in the measured data. Stogryn (1978) recognized that the problem of inverting a series of antenna temperatures to yield a brightness temperature was mathematically identical to that of inverting antenna temperatures (measured in either the microwave or infrared regime) to yield an atmospheric temperature profile. Research in this field had already shown that attempting to obtain higher resolution in the retrieved profiles could result in the amplification of noise. This trade-off between noise and resolution was recognized by Backus and

Gilbert (1970) in their geophysical research. Stogryn's application of the Backus-Gilbert matrix inverse method to the problem of estimating brightness temperatures seeks to minimize noise amplification by the use of a tuning parameter. We have implemented the technique in conjunction with SSM/I measurements in such a fashion so as to objectively determine the channel-dependent tuning parameters. A detailed presentation of the method and its validation was presented by Farrar and Smith (1992). [Other SMMR and SSM/I applications have been given by Olson (1986) and Robinson et al. (1992); however, the former study utilized an empirically determined blurring function rather than the actual antenna gain function, and the latter study (which also uses the Stogryn technique) obtained the tuning parameter from synthetic data.] A brief discussion of the method follows.

Consider a set of  $N$  measurements, whose antenna patterns overlap, which are to be utilized to determine the brightness temperature for some point at  $\rho_0$  on the earth's surface. As this problem is mathematically identical to that considered by Backus and Gilbert (1970), Stogryn (1978) applied their method of solving a system with a linear combination of the  $N$  antenna temperatures, which approximates  $T_B(\rho_0)$ :

$$T_B(\rho_0) = \sum_{i=1}^N c_i T_{A_i}. \quad (1)$$

Now an antenna temperature is defined as the product of the brightness temperature field and the antenna gain function, integrated over the region  $E$  viewed by the instrument; that is,

$$T_{A_i} = \int_E \bar{G}_i(\rho) T_B(\rho) dA, \quad (2)$$

and the antenna gain is normalized such that  $\int \bar{G}_i dA = 1$ , the expression for  $T_B(\rho_0)$  in Eq. (1), may be re-written as

$$T_B(\rho_0) = \sum_{i=1}^N c_i \bar{T}_{B_i}, \quad (3)$$

where  $\bar{T}_{B_i}$  are a series of brightness temperatures and the overbar indicates a weighted average obtained by integration over the gain function. As it is not possible to produce a set of  $c_i$  yielding a perfect solution for  $T_B(\rho_0)$ , the problem reduces to finding a set of  $c_i$  that most closely estimates  $T_B(\rho_0)$ .

The matrix inverse method employed by Stogryn (1978) to solve for the set of coefficients  $c_i$  attempts to balance the trade-off of resolution and noise by minimizing a quantity  $Q$  with a normalization constraint ( $\sum c_i = 1$ ); that is,

$$Q = Q_R \cos \gamma + w Q_N \sin \gamma, \quad (4)$$

where  $Q_R$  is a function of  $c_i$  and resolution information (i.e., antenna gain),  $Q_N$  is a function of  $c_i$  and instru-

ment noise,  $w$  is chosen to ensure that  $Q_R$  and  $Q_N$  are dimensionally consistent, and  $\gamma$  is referred to as the tuning parameter. The tuning parameter allows emphasis to be placed on resolution or noise as it is varied from 0 to  $\pi/2$ , respectively. Poe (1990) used this same method to interpolate the low-frequency SSM/I measurements to the 85-GHz grid spacing while maintaining their original spatial resolution. As the resolution was not increased, the effects of noise production were small and were neglected by choosing  $\gamma = 0$ . Since our method leads to resolution increase, the effects of noise amplification must be considered.

#### 4. Objective specification of tuning parameter

As indicated above, the tuning parameter  $\gamma$ , which attempts to balance the trade-off between resolution and noise, remains unaccounted for in the solution vector. Since there is no a priori rule that can objectively determine this parameter, we choose  $\gamma$  on the basis that the intercorrelation between the deconvolved channel and the next highest frequency channel is maximized over a selection of pixels that exhibit cross-channel consistency. As pointed out in Farrar and Smith (1992), cloud-free coastline areas represent ideal choices for obtaining this type of consistency. Cloud areas containing precipitation represent poor choices for seeking optimal  $\gamma$ 's since the scattering effects of precipitation-sized particles at the higher frequencies (e.g., 85 GHz) can lead to radiation losses and minimum values, while the same precipitation regions may exhibit little scattering at the lower frequencies and appear as relative maximum values due to elevated emission effects. This negative correlation, when coupled with the remainder of the scene, which can be positively correlated, would then contaminate the cross-channel correlation approach in determining the optimal  $\gamma$ 's.

Another consideration in selecting data regions for determining tuning parameters is that there must be sufficiently high brightness temperature gradients such that the blurring effects in the lower-resolution channels may be detected. Coastlines are also good choices in this regard because large gradients are present at the boundaries between the high-emittance (warmer) land and low-emittance (relatively colder) water (see Olson et al. 1986). Hence, cloud-free coastline scenes were chosen to derive the  $\gamma$ 's with the cross-correlation technique. The cases were selected from four locations frequented by tropical storms: western Pacific, eastern Pacific, Caribbean, and Indian Ocean coastlines.

After determining the best  $\gamma$  at each SSM/I channel for all selected coastline cases, the results were averaged by channel to yield a set of coefficients (given in Table 1) to be applied to any arbitrary case. Since it can be shown that the determination of  $\gamma$  for a given channel is somewhat scene dependent and that a deconvolution result is sensitive to the choice of  $\gamma$ , the utilization of

TABLE 1. Average values of tuning parameter  $\gamma$  for 19-, 22-, and 37-GHz SSM/I channels.

Channel	$\gamma$
37 GHz (V)	$0.53 \pi/2$
37 GHz (H)	$0.48 \pi/2$
22 GHz (V)	$0.13 \pi/2$
19 GHz (V)	$0.13 \pi/2$
19 GHz (H)	$0.08 \pi/2$

average values degrades the technique from optimum performance for all cases. Hence, although there are no universal best choices for the  $\gamma$ 's, our tests indicate that the use of averaged coefficients is optimal for cases where the cross-correlation technique should not be directly applied, such as precipitation scenes.

### 5. Selection of tropical cyclone cases

The dataset utilized for the selection of the tropical cyclone cases consisted of seven weeks of worldwide SSM/I brightness temperature measurements, from 10 July to 27 August 1987. The selection of cases was performed by a systematic search of overpasses of recorded named storms. Cases were selected on the basis that at least five overpasses providing more than 50% coverage while over water were available over a storm's lifetime. This search was aided by the time-location history documented for each prevalent tropical storm region. Hoffman et al. (1987) provided the information for the eastern hemisphere cyclones, while those for the western hemisphere were produced by Case and Gerrish (1988) for the Atlantic and by Cross (1988) for the eastern Pacific. These records simplified the search for good cases, since we had nearly exact information to determine where and when to look.

The only remaining problems were due to the nature of the near-polar orbits of the DMSP (Defense Meteorological Satellite Program) spacecraft on which the SSM/I instruments are flown and the nature of the SSM/I scan pattern. Since these satellites are in sun-synchronous orbits, they pass over a given spot once every 12 h, while the width of the radiometer scan swath is only 1394 km, leaving gaps in the coverage that increase as the latitude decreases. For these reasons, storm

monitoring can only be done intermittently, and for a number of overpasses only a portion of the storm can be sampled (if it is not missed altogether). Although these problems were present throughout the life of all of the storms examined, the degree of the problem varied. For some cases, many consecutive overpasses viewed a storm well, only to miss the next several in a row. In other cases the storm could be viewed for nearly all overpasses, but only partially, as it consistently missed the eye. Still for other cases, the majority of a storm's life cycle could be viewed, only to miss the crucial time when the storm was at or near its maximum strength. In selecting the cases used for this study, we took all of these considerations into account. Cases that had inadequate coverage during a particular time period of the storm, cases that had many consecutive missed overpasses, and cases that consistently sampled only the periphery of the storm while missing the eye-wall were not used. The remainder of the cases that passed these screening tests were then deemed adequate to represent the life cycle of each storm. The screening procedure resulted in seven cases being selected—all are adequate for a complete temporal analysis of the precipitation cycle. The names, general locations, dates, and number of useful overpasses are given in Table 2.

### 6. Impact of deconvolution on retrieval algorithms

The quantitative effect of the deconvolution procedure on the actual brightness temperatures was evaluated in terms of its impact on six microwave precipitation retrieval algorithms applied to the tropical cyclone cases identified in the previous section. Three of these algorithms use only 19-GHz and/or 37-GHz brightness temperature data. The first of these is the single-channel emission-based algorithm for unpolarized 19-GHz measurements described by Smith and Mugnai (1988), hereafter SM-RM. The second is the scattering-based algorithm of Spencer et al. (1989), hereafter SEA-RM, which utilizes polarization differences at 37 GHz to measure the scattering effects of precipitation in terms of polarization-corrected brightness temperatures (PCTs), from which rain rates are then derived based on a regression equation. The third is that of Hinton et al. (1992), hereafter HEA-RM, a physical-statistical regression algorithm developed for

TABLE 2. Description of tropical cyclone cases.

Name	Status	Region	Dates	Number of overpasses
Arlene	hurricane	Atlantic	13–24 Aug	8
Betty	supertyphoon	west Pacific	9–16 Aug	8
Cary	typhoon	west Pacific	13–21 Aug	10
Greg	hurricane	east Pacific	28 Jul–2 Aug	5
Hillary	hurricane	east Pacific	1–9 Aug	9
Thelma	supertyphoon	west Pacific	10–14 Jul	7
Wynne	typhoon	west Pacific	22–30 Jul	10

the *Nimbus-7* SMMR instrument. It is actually a weighted average of four single-channel algorithms (developed for 18H, 18V, 37H, and 37V GHz), where the weights are determined from the response of each channel to the magnitude of the detected rain rate. Note that while the regression equations were developed for the SMMR frequencies of 18 and 37 GHz, they were used with SSM/I data measured at 19.35 and 37 GHz. Hence, the results for this algorithm should be considered in terms of the effects of the deconvolution procedure rather than a fully quantitative evaluation of the rainfall retrieval itself when SSM/I data are employed.

The other three algorithms employed in this study utilize both lower-frequency channels and the high-frequency 85-GHz channels. The first of these is the method developed for operational use at the Department of Defense's centralized weather forecasting facilities referred to as CalVal (1991), hereafter CalVal-RM. This is a nonlinear multiple regression scheme utilizing all four SSM/I frequencies (but only five of seven channels), in which the regression coefficients were derived from radar-retrieved rain-rate data obtained in conjunction with an SSM/I training dataset. The second is that of Kummerow et al. (1991), hereafter KEA-PR, which is based on the numerical inversion of a forward radiative transfer model used to generate a most probable vertical rain profile selected from a set of 25 possible rain profiles (derived from aircraft radar). The third is the cloud model-based profile inversion scheme of Smith et al. (1992a), Mugnai et al. (1993), and Xiang et al. (1992), hereafter SMX-PR, which utilizes all but the SSM/I 22-GHz V-pol (vertical polarization) channel in the inversion procedure. Detailed descriptions of all six algorithms are presented in the Appendix. In the preceding acronyms, the first group of letters denotes the basic reference(s) (as given above) and the second group of letters indicates whether the algorithm is of the rain-map variety (RM) or the profile variety (PR). In this nomenclature, a rain-map algorithm produces a single rain rate for a column (assumed to apply to the surface), whereas a profile algorithm generates vertically resolved rain rates along a column (including the surface). For this study, only surface rain rates from the two profile algorithms are utilized. The algorithm naming convention is summarized in Table 3 along with all pertinent references.

Initially, the deconvolution procedure was applied to all of the scenes for the different storm cases, yielding two sets of raw and deconvolved brightness temperatures. (All land areas were screened from the scenes so that the comparisons consider only oceanic rainfall.) Then both datasets were used as input to each of the six rainfall algorithms to produce six sets of raw and deconvolved rain rate maps. This process was performed for all overpasses for each of the tropical storm cases given in Table 2. It should be noted before pro-

TABLE 3. Algorithm naming convention and relevant references.

Algorithm name	References
SM-RM	Smith and Mugnai (1988) Mugnai and Smith (1988)
SEA-RM	Spencer et al. (1989)
CalVal-RM	CalVal (1991)
HEA-RM	Hinton et al. (1992) Hinton et al. (1990)
KEA-PR	Kummerow et al. (1991) Kummerow et al. (1989)
SMX-PR	Smith et al. (1992a) Smith et al. (1992b) Smith et al. (1994) Mugnai and Smith (1993) Xiang et al. (1992)

ceeding that three of the six algorithms were not designed with the idea that deconvolved brightness temperature data would be used as input for making rainfall estimates; these are the SEA-RM, HEA-RM, and CalVal-RM algorithms. Therefore, this analysis should not be used to detract from the overall quality of the algorithms based on their performance with the spatially enhanced data. Instead, as indicated in the Introduction, the analysis is designed to better understand the magnitude of the impact of deconvolution on different algorithm designs.

#### a. Analysis of Supertyphoon Thelma

We first conduct a detailed examination of one of the cases—Supertyphoon Thelma—to develop an in-depth understanding of how the various algorithms respond as the input data are switched between raw and deconvolved brightness temperatures. Thelma was a major west Pacific typhoon during the 1987 tropical storm season. Seven overpasses between 10 and 14 July were identified for the analysis. A depiction of the storm at 2131 UTC 11 July at 85 GHz (V-pol) is shown in Fig. 1; the time of this overpass is closest to the time the storm was at peak intensity according to the Joint Typhoon Warning Center (JTWC). Rain-rate maps of the same scene derived from the six precipitation algorithms are presented in Figs. 2a,b. The left-hand panels show the retrievals from the raw brightness temperature data; the right-hand panels show the retrievals from the deconvolved data. Qualitative examination of each of these pairs of images immediately reveals the overriding positive effect of the deconvolution method. The graininess apparent in the raw versions is largely eliminated in the deconvolved versions leading to better enhancement of the rainbands as well as tightening of the gradients between precipitating and nonprecipitating areas. Such improvements in the definition of terrestrial geographical features has been dis-

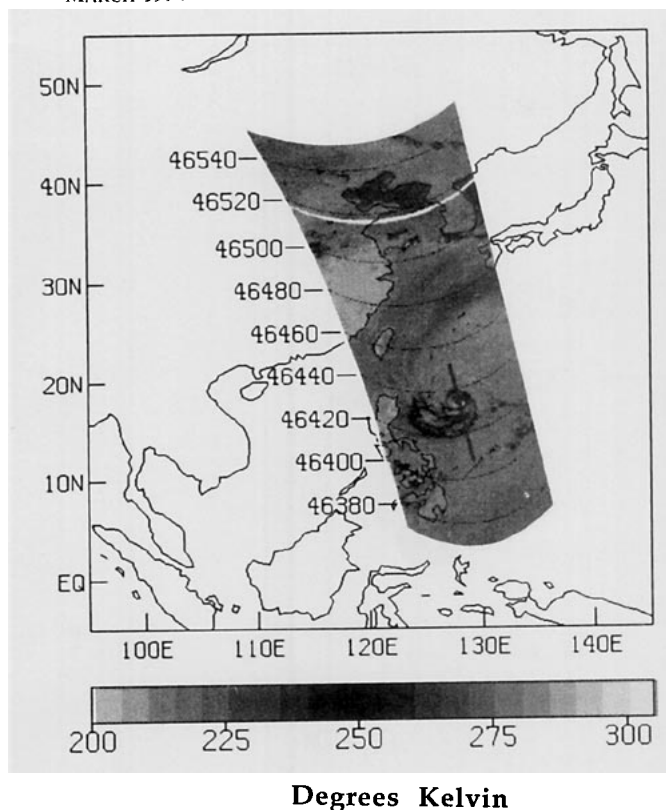


FIG. 1. Ascending node microwave image at 85 GHz (V-pol) of Supertyphoon Thelma in the western Pacific at approximately 2131 UTC (0731 LST) 11 July. A gray-shade scale for brightness temperature is given at the bottom of the figure. Scan line counts are indicated in steps of 20 (scans run from right to left). The straight black line through the storm core represents a transect path given special attention in a cross-sectional analysis (see Figs. 5a,b).

cussed in Farrar and Smith (1992). Differences in spatially distributed rain rates between the raw and deconvolved cases are quite apparent in some of the algorithms but not so clear-cut in others. The analysis given below will detail these differences quantitatively.

The quantitative evaluation of the effect of the deconvolution procedure on the rain-rate retrieval algorithms will be given mostly in terms of its impact on area-averaged rain rates, although pixel-level impacts are tabulated in Table 5. After the rain-rate maps were calculated for each overpass of each of the selected storm cases, they were integrated over the entire storm domain to yield a domain-averaged rain rate for the scene. It is clear from Fig. 2 that the different algorithms produced different results vis à vis the intensity around the eyewall and within the convective spiral bands, as well as the stratus and drizzle areas surrounding the bands and well away from the eye. Therefore, it is not surprising that the area-integrated results will differ from algorithm to algorithm. However, the focus here is on explaining the sensitivity of each of the algorithms to spatial enhancement rather than the relative differences in total rainfall between algorithms (this problem

will be addressed in a future study). In first conducting the analysis for Thelma, we provide an account of each rainfall algorithm in terms of the domain-averaged precipitation history of the storm.

It should be noted from Fig. 2 that the HEA-RM algorithm produces low but nonzero values of rain rate for the entire storm domain (this may be the result of using 19.35-GHz input in the 18-GHz equations). The CalVal-RM algorithm also produces rain over much of the domain. Since this is likely unrealistic and the other algorithms do not exhibit this property, a comparison of rain rates involving all of the methods may be biased by this type of difference. Hence, the use of minimum rain-rate cutoff values was introduced into the analysis. In this approach, any value of rain rate less than a specified cutoff is neglected in the calculation of domain-averaged rain rate. Four cutoffs of 0, 1, 3, and 5 mm h<sup>-1</sup> were selected. This not only allows a more thorough comparison between the different methods but also allows the effect of the deconvolution method on more intense rain areas to be isolated.

For the sake of brevity, graphic representation of domain-averaged rain-rate time series has been limited to Supertyphoon Thelma. Tables 4–6 will be used to summarize results for the other storm cases along with Thelma. Figure 3a shows the domain-averaged rain rates for the six algorithms throughout the seven Thelma overpasses, for the four different rain-rate cutoffs based on the raw measurements. Figure 3b shows similar results based on the deconvolved measurements.

The first time series given on the left in the two figures are produced from the SM-RM algorithm. This is a relatively simple, single-frequency emission-type algorithm based on the 19-GHz channel (at which frequency the influence of absorption–emission dominates the  $T_B$ –RR relationship up to rain rates of about 12 mm h<sup>-1</sup>). The structure of the  $T_B$ –RR relationship used for this algorithm is shown in Fig. 4. The abscissa is plotted in log coordinates in order to emphasize that brightness temperature response to rain rate is highly nonlinear; see Wilheit et al. (1977) and Smith and Mugnai (1988) for more thorough discussions. As shown by Smith and Kidder (1978), lack of beam filling by necessity will lead to underestimation of rainfall with this type of relationship if the bulk of the rain rates lies to the left of the maximum in the double-valued functional relationship. Therefore, the associated algorithm would be expected to be sensitive to deconvolution, and in theory, retrievals based on spatially enhanced data should exhibit higher rain rates. Figure 3a indicates several interesting features for this algorithm. The maximum rain-rate peak for the third overpass coincides with the time of maximum intensity reported by Hoffman et al. (1987) and grows as expected as the higher rain-rate cutoffs are imposed. However, the sharp minimum left of this peak is lower than it should be because the storm coverage on that



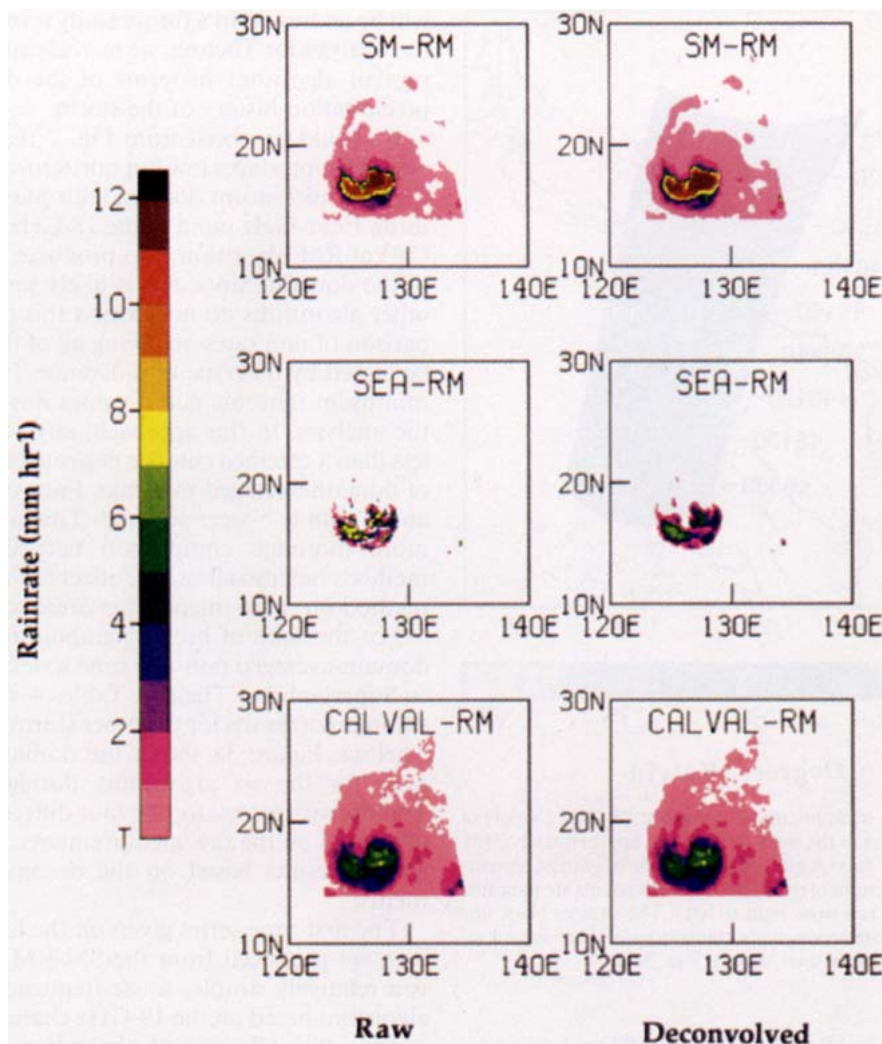


FIG. 2a. Rain-rate maps for the 2131 UTC 11 July Thelma overpass for both raw (left panels) and deconvolved (right panels) measurements based on the SM-RM, SEA-RM, and CalVal-RM algorithms. A gray-shade scale for rain rate ( $\text{mm h}^{-1}$ ) is given at the bottom of the figure.

particular overpass missed much of the eyewall and thus the contribution by heavy rainfall areas. The peak for the sixth overpass, which emerges at higher cutoff values, is somewhat of an aberration, which occurs due to the very small number of pixels that exceed the higher rain rates. Another interesting feature is the overall behavior of the time series as a function of the rain-rate cutoff. There is a fairly significant separation between the graphs for the first two cutoffs, that of 0 and  $1 \text{ mm h}^{-1}$ . This is due to the large areas of light rain rate (less than  $1 \text{ mm h}^{-1}$ ) away from the central eyewall (seen in Fig. 2a) and their contribution to the domain average.

The effect of deconvolution on retrieved rain rates for the SM-RM algorithm is illustrated in Fig. 3b, where the domain-averaged values exceed those retrieved from the raw data by a mean value of 3.1% for the 0

$\text{mm h}^{-1}$  cutoff and 3.5% for the  $1 \text{ mm h}^{-1}$  cutoff, as indicated in Table 4. (This table provides the time means over all overpasses of a given storm case of the domain-averaged percentage differences between raw and deconvolved derived rain rates with respect to all algorithms for all storms.) The magnitudes of these time-space-integrated differences are not exceptional, although domain-averaged raw deconvolved differences at individual overpass times are as high as 7.1%, and pixel-level raw deconvolved rain-rate differences in the course of the storm exceed  $7.5 \text{ mm h}^{-1}$ . Table 5 provides summaries of the maximums, minimums, and minimum absolute values of domain-averaged percentage differences over all overpass times with respect to each algorithm for each storm case. Furthermore, as Tables 4 and 5 indicate, two other storm cases exhibit time mean differences exceeding 12% with do-



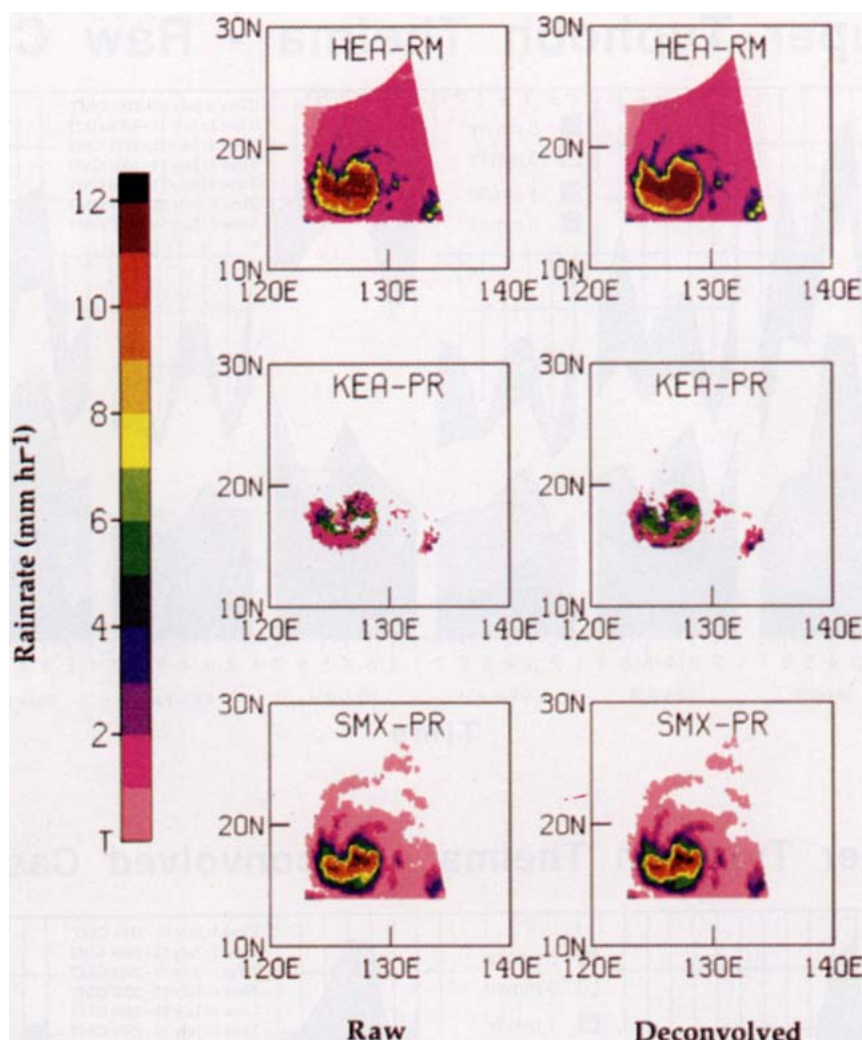


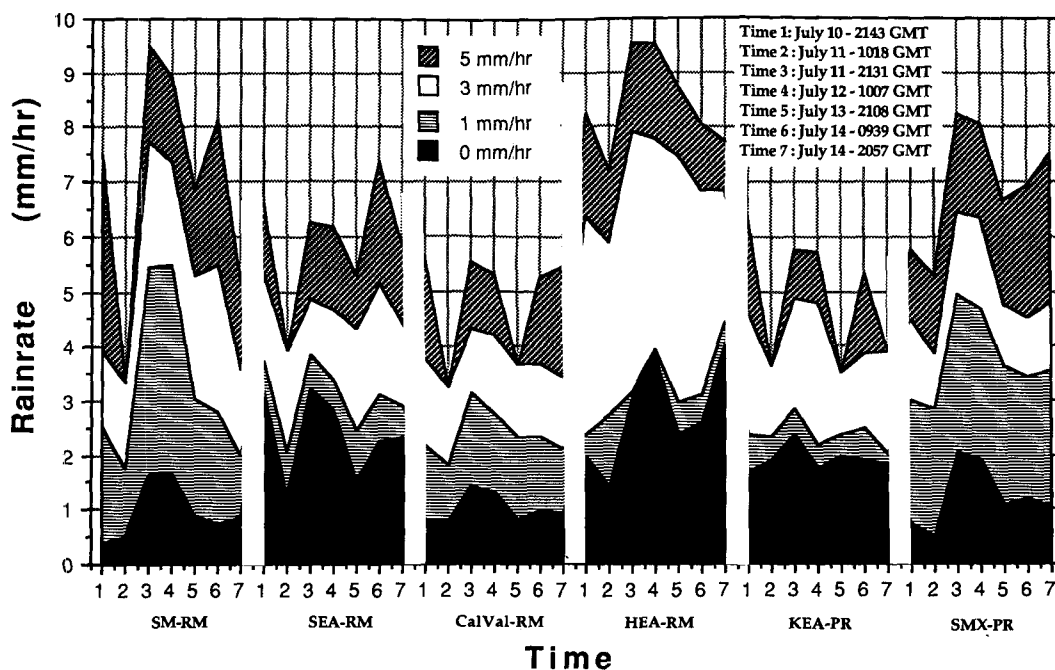
FIG. 2b. Same as Fig. 2a except for the HEA-RM, KEA-PR, and SMX-PR algorithms.

main-averaged differences at individual overpass times as high as 63% for the  $0 \text{ mm h}^{-1}$  cutoff of Wynn. Moreover, it must be recognized that the time-space-integrated differences must be taken with respect to fairly large areas over fairly long time periods, so that the total rain volume differences between the raw and deconvolved retrievals are significant for time-space-integrated differences on the order of 5%. The other salient point is that all domain-averaged differences for the SM-RM algorithm are positive (deconvolved greater than raw results), as would be expected from the nonlinear transform properties of the dominant portion of the  $T_B$ -RR relationship. Because of the deblurring effect of the deconvolution process, smaller areas of rainfall not evident in the raw data undergo brightness temperature enhancement and thus nonlinear amplification of rain rate through the relationship given in Fig. 4.

The next analysis is conducted for the single-frequency (37 GHz) SEA-RM scattering algorithm. The

same peaks in rain rate seen in the previous algorithm are observed with this method, with the exception that at the two higher cutoffs the peak for the sixth overpass emerges as the absolute maximum. The major change with respect to the previous algorithm are in the magnitude of the percentage differences between the raw and deconvolved results. The rain rates derived from the raw brightness temperatures are often in excess by more than 10% (up to 61%) than those derived from the deconvolved data in terms of time-space averages (Table 4) and up to 100% for space averages alone (Table 5) when considering Thelma and all other storms at any selected cutoff. The largest pixel-level rain-rate differences exceed  $10 \text{ mm h}^{-1}$ . However, this behavior cannot be attributed to the rainfall algorithm, since the relationship between rain rate and the PCT parameter is linear (as indicated in the Appendix). Thus, a perfect energy-conserving spatial deconvolution scheme should preserve the PCT rain rates exactly. The consistent negative differences arise because the

## Super Typhoon Thelma - Raw Case



## Super Typhoon Thelma - Deconvolved Case

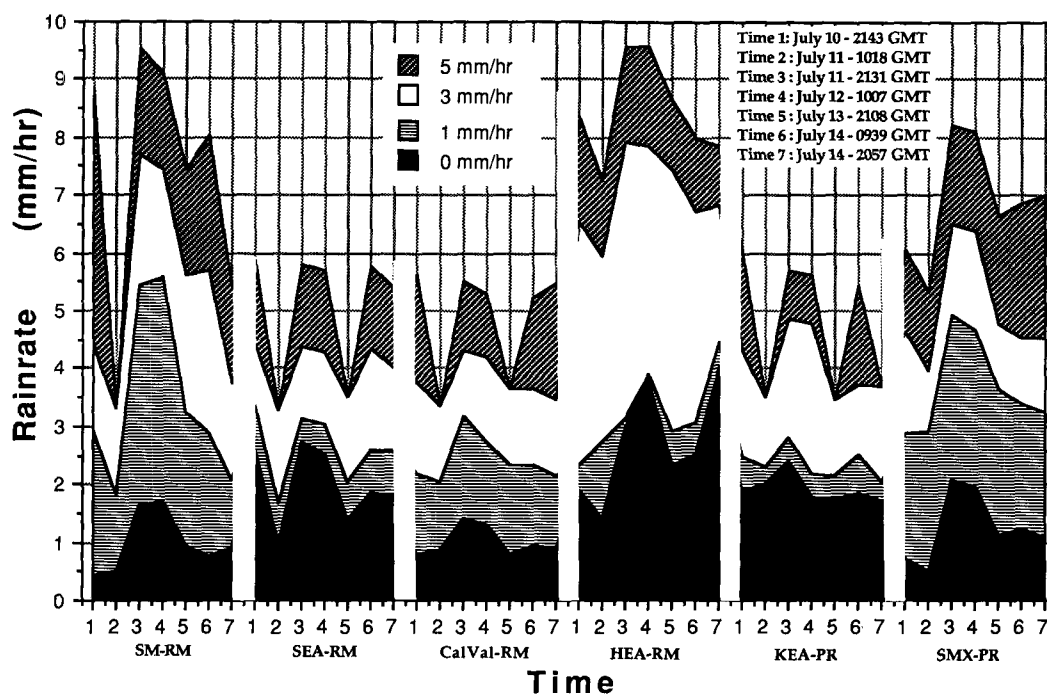


FIG. 3. (a) Domain-averaged rain rates for the six retrieval algorithms throughout the seven overpasses of Supertyphoon Thelma. The results are based on raw measurements. Each algorithm time series is repeated for four different rain-rate cutoffs; shading is used to indicate the various cutoffs (0, 1, 3, 5 mm h<sup>-1</sup>). For example, if the cutoff is 3 mm h<sup>-1</sup>, all rain rates less than this value are excluded from the domain average. (b) Same as (a) except for deconvolved measurements.

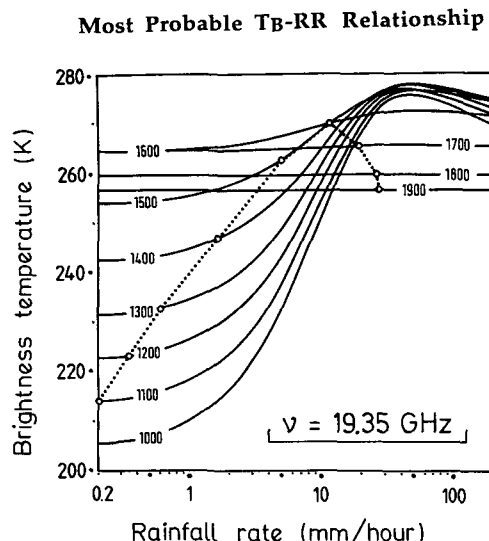


FIG. 4. Depiction of Smith and Mugnai (1988) 19-GHz most probable brightness temperature–rain rate algorithm (dotted line). The solid lines indicate a family of  $T_B$ -RR relationships for a sequence of cloud model times (given in seconds past initial point) in the course of a convective storm simulation from which the most probable  $T_B$ -RR relationship was derived.

deconvolution procedure is carried out independently for each channel and since the PCT is a function of the difference between the vertical and horizontal polarizations, the deconvolution itself introduces a spurious brightness temperature bias. The deconvolution-induced bias in turn biases the rain rates. Because the technique for finding an optimum tuning parameter must be conducted independently for each separate polarization, the values of  $\gamma$  for 37-GHz V-pol and H-pol are different, as seen in Table 1. To determine whether the brightness temperature bias was actually produced by these tuning parameter differences, the test cases were rerun with the value of  $\gamma$  for the vertical polarization set equal to that of the horizontal polarization. While the numerical values in Tables 4 and 5 changed somewhat, the overall mean values remained relatively constant. Hence, the bias is produced by other factors related to the two polarized channels, such as differences in their gain functions and channel noise. This demonstrates that preserving consistency between polarizations in the deconvolution method itself can be important for certain applications. This will be the topic of a future study.

One final notable aspect of the SEA-RM is that it does not detect stratiform or light, warm-type rain situations. This can be seen in the precipitation pattern illustrated in Fig. 2a, where only the major convective band and eyewall are depicted as rain areas. The surrounding areas of lighter rain (seen in the SM-RM, CalVal-RM, HEA-RM, and SMX-PR algorithms) do not contain enough ice or large rain drops to induce a scattering signature cold enough to fall below the rain

threshold of 270 K. This explains why the overall magnitudes of the SEA-RM domain-averaged rain rates, noted in Figs. 3a,b, are generally smaller than those produced by algorithms that are emission based or equally sensitive to emission and scattering effects. In terms of comparing the impact of deconvolution on different algorithms, this draws attention to the fact that each algorithm has its own unique response to the ensemble of precipitation microphysics contained within a given storm. Thus, an evaluation of deconvolution sensitivity for a given algorithm must not only consider the frequencies and basic techniques it employs but also the type of precipitation and cloud hydrometeors to which it responds.

The third technique under consideration is the three-frequency, five-channel CalVal-RM algorithm. Figures 3a,b indicate some similarity between the performance of this algorithm and those of SEA-RM and KEA-PR in both the general magnitude of the rain rates and in the behavior of the two peaks. The major difference is seen in the relatively small mean rain rates of the 0 mm h<sup>-1</sup> cutoff case. In fact, this algorithm produces the lowest average rain rates of the six algorithms tested when all nonzero rain rates are considered. As mentioned in the Appendix, this is most likely related to the lack of enough high-rain-rate samples in the radar dataset used to derive the regression coefficients for the algorithm. By the same token, the domain-averaged rain rates for the 3 and 5 mm h<sup>-1</sup> cutoffs are quite similar to those of SEA-RM and KEA-PR, so that it would appear if the low overall average represents a bias, it would be restricted to the light rain rates being biased low. However, this analysis can be used only to speculate on the behavior of the rain-rate magnitudes relative to the other algorithms, not to ascertain that biases actually exist.

What is clearly evident in the CalVal-RM results is that the algorithm is nearly impervious to the application of the deconvolution procedure. An examination of Table 4 for the Thelma case, along with the other storm cases, demonstrates that the largest time mean difference due to deconvolution for the 0 mm h<sup>-1</sup> cutoff is 4.2% for Arlene, with the six other storms exhibiting differences less than 1%. Moreover, the differences have both positive and negative signs, implying an even smaller overall bias. This result could be viewed in either of two ways. On the one hand, this might be considered a negative result because it suggests the algorithm cannot be improved with higher-resolution data. On the other hand, it might be considered a positive result because the algorithm can be applied directly to raw data without concern for mismatched footprints (this might have been expected since the algorithm is based on an empirical regression procedure utilizing raw brightness temperatures in the training dataset). In fact, neither of these viewpoints is completely accurate. The correct interpretation is that at the domain-averaged scale, as indicated in Table 5, the algorithm

TABLE 4. Time means of domain-averaged percentage differences between deconvolved and raw derived rain rates with respect to each algorithm for each storm case at four minimum rain-rate cutoff values. Positive differences indicate that deconvolved derived rain rates exceed raw derived rain rates.

Method	Storm	Minimum rain-rate cutoff values			
		0 mm h <sup>-1</sup>	1 mm h <sup>-1</sup>	3 mm h <sup>-1</sup>	5 mm h <sup>-1</sup>
SM-RM	Arlene	4.7	3.1	11.0	12.8
	Betty	3.5	4.2	3.7	2.8
	Cary	4.3	3.9	3.0	1.9
	Greg	3.4	2.2	1.9	2.8
	Hillary	4.8	3.2	5.5	4.7
	Thelma	3.1	3.5	3.1	5.2
	Wynne	12.3	17.9	14.4	12.5
SEA-RM	Arlene	-25.9	-19.8	-5.3	-4.5
	Betty	-5.9	-4.2	-6.2	-6.2
	Cary	-8.4	-6.3	-6.2	-6.7
	Greg	-60.9	-24.7	-4.1	-3.2
	Hillary	-10.0	-10.4	-13.0	-17.0
	Thelma	-13.0	-8.7	-22.4	-20.2
	Wynne	-11.3	-11.5	-10.0	-22.4
CalVal-RM	Arlene	4.2	1.4	0.3	-0.1
	Betty	-0.7	0.3	0.1	0.0
	Cary	0.3	0.2	-0.1	0.6
	Greg	0.1	0.7	-0.1	0.1
	Hillary	-0.2	0.5	-0.1	-0.1
	Thelma	-1.0	0.1	0.0	-0.1
	Wynne	0.4	0.0	-0.6	0.6
HEA-RM	Arlene	-0.5	-1.1	-1.0	-0.4
	Betty	-0.5	-0.6	-0.2	0.5
	Cary	-0.6	-0.6	-0.2	0.4
	Greg	-0.3	-0.4	-0.0	0.4
	Hillary	-0.5	-0.8	-0.4	0.6
	Thelma	-0.6	-0.6	0.7	0.6
	Wynne	-0.4	-0.7	0.3	1.1
KEA-RM	Thelma	0.1	-0.6	-0.2	0.4
SMX-RM	Arlene	3.7	2.7	0.8	1.0
	Betty	1.8	1.8	1.0	1.5
	Cary	2.0	2.3	1.4	1.2
	Greg	1.6	0.8	1.0	2.6
	Hillary	2.4	1.4	1.3	0.8
	Thelma	1.8	0.5	1.5	0.7
	Wynne	1.5	1.8	1.2	1.6

is not particularly sensitive to deconvolution, whereas at the pixel scale, rain-rate differences can exceed 5 mm h<sup>-1</sup>. However, since these differences take on both positive and negative values in near-equal proportion, the deconvolution procedure does not produce a meaningful bias in the time-space-integrated retrievals for all storms (see Table 6).

The HEA-RM algorithm, representing the weighted combination of four separate single-channel regressions, was developed for the four polarized channels at 18 and 37 GHz on the *Nimbus-7* SMMR instrument (see Appendix). We have applied it to SSM/I measurements in which the low-frequency channel is at a slightly higher frequency (19.35 GHz), and thus, it cannot be expected to perform optimally. The time series of domain-averaged rain rate seen in Figs. 3a,b exhibit some similarities to the SM-RM algorithm at

the two higher cutoffs but are dramatically different at the two lower cutoffs. For the Thelma case, the HEA-RM algorithm produces the largest domain-averaged rain rates for the 0 mm h<sup>-1</sup> cutoff. For reasons not completely understood, the false peak at the sixth overpass is observed for the two lower cutoffs but then disappears for the two higher cutoffs, unlike the other five algorithms. Another obvious feature is the overprediction of light rainfall; that is, Fig. 2b shows that the entire storm domain is experiencing rainfall. This means one or more of the nonzero rain-rate brightness temperature threshold values of the method are set too low. Of course if the problem stems from the values used in the 18-GHz regression equations, they would, by definition, be too low for the 19.35-GHz SSM/I measurements because the latter frequency has a higher water vapor absorption coefficient. Notwithstanding

TABLE 5. Maximums, minimums, and minimum absolute values (with that value's sign given in parentheses) of domain-averaged percentage differences (for 0 mm h<sup>-1</sup> cutoff) from all overpasses of each storm case for all algorithms.

Method	Storm	Domain-averaged percentage difference		
		Maximum	Minimum	Minimum absolute value
SM-RM	Arlene	12.4	0.9	0.9 (+)
	Betty	6.9	0.8	0.8 (+)
	Cary	7.2	0.3	0.3 (+)
	Greg	6.7	0.8	0.8 (+)
	Hillary	5.9	0.9	0.9 (+)
	Thelma	7.1	0.8	0.8 (+)
	Wynne	63.3	1.0	1.0 (+)
SEA-RM	Arlene	-6.2	-100.0	6.2 (-)
	Betty	6.9	-15.8	1.4 (-)
	Cary	8.1	-18.6	6.1 (-)
	Greg	-13.7	-100.0	13.7 (-)
	Hillary	5.4	-42.7	0.3 (-)
	Thelma	2.7	-24.9	2.7 (+)
	Wynne	-0.6	-35.9	0.6 (-)
CalVal-RM	Arlene	7.1	2.5	2.5 (+)
	Betty	0.4	-3.3	0.0
	Cary	0.5	-1.1	0.0
	Greg	2.0	-1.5	0.4 (-)
	Hillary	2.1	-2.7	0.0
	Thelma	0.1	-2.2	0.1 (+)
	Wynne	6.0	-3.9	0.0
HEA-RM	Arlene	1.3	-1.3	0.1 (+)
	Betty	0.1	-0.8	0.1 (+)
	Cary	-0.3	-1.1	0.3 (-)
	Greg	0.0	-0.8	0.0
	Hillary	0.1	-1.2	0.0
	Thelma	-0.2	-1.2	0.2 (-)
	Wynne	-0.1	-0.8	0.1 (-)
KEA-PR	Thelma	9.3	-10.0	2.5 (+)
SMX-PR	Arlene	6.2	1.6	1.6 (+)
	Betty	4.8	-4.8	1.7 (+)
	Cary	3.6	0.7	0.7 (+)
	Greg	2.3	0.8	0.8 (+)
	Hillary	5.0	0.4	0.4 (+)
	Thelma	3.5	0.3	0.3 (+)
	Wynne	4.9	-7.8	1.9 (+)

the frequency discrepancies between SMMR and SSM/I, the rain-rate values for the regions in question are quite small and are largely eliminated in the 1 mm h<sup>-1</sup> cutoff category. Note that rain rates below 1 mm h<sup>-1</sup> contribute very little to the 0 mm h<sup>-1</sup> cutoff average as evident by the near proximity of the time series at these two cutoffs.

As with the CalVal-RM scheme, the HEA-RM algorithm is basically insensitive to the deconvolution process, as seen in Table 4 (the largest time mean differences are on the order of 1%). Whereas the differences between rain rates derived from raw and deconvolved brightness temperatures of Thelma exceed 7.5 mm h<sup>-1</sup> at individual pixels for the SM-RM 19-GHz algorithm, the largest differences for this algorithm are

less than 4 mm h<sup>-1</sup>. This is apparently due to the interaction of the separate 19- and 37-GHz regressions, which are combined to form the final brightness temperature-rain rate relationship. Even though this algorithm takes the form of an emission algorithm at both frequencies (rain rates monotonically increase with brightness temperature warming in all four channels), the weighting procedure produces a more linear response than a standard emission algorithm resulting in less sensitivity to nonhomogeneous beam filling. Another possible reason the rain rates are not as sensitive to deconvolution could stem from the maximum allowable rain rate used in the separate regressions. Each regression is devised so that the rain rate cannot exceed 12 mm h<sup>-1</sup>. That threshold is exceeded for some portions of Thelma. In those areas, the deconvolved and raw rain rates are both set to the threshold and therefore the deconvolution procedure can have no measurable effect. The value used for the maximum threshold was based on prescribing physical parameters consistent with precipitation over the Indian Ocean in the radiative model used to develop the algorithm, parameters that may not embody the higher rain rates present in the typhoon cases examined in this study.

The behavior of the seven-channel multispectral KEA-PR algorithm is not as straightforward to interpret as the prior algorithms. This algorithm is also insensitive to deconvolution with respect to time means (as seen in Table 4, the largest time mean difference for Thelma is -0.6%). Furthermore, time mean differences vary in sign as the cutoff changes (Table 4), while domain-averaged differences vary in sign as the time of overpass changes (Table 5). This demonstrates the same basic insensitivity to deconvolution shown by the two previous multispectral algorithms (CalVal-RM and HEA-RM) with respect to time-space-integrated retrievals.

However, Table 5 also shows that the domain-averaged differences for the individual overpasses are larger for this algorithm in comparison to the previous two (on the order of 10%), and pixel-level rain-rate differences can exceed 7 mm h<sup>-1</sup>. In this regard, the relatively small time mean values given in Table 4 are

TABLE 6. Grand-averaged percentage differences (average for all storms of time means of domain-averaged percentage differences) with respect to each algorithm for four minimum rain-rate cutoff values.

Method	0 mm h <sup>-1</sup>	1 mm h <sup>-1</sup>	3 mm h <sup>-1</sup>	5 mm h <sup>-1</sup>
SM-RM	5.2	5.4	6.1	6.1
SEA-RM	-19.3	-12.2	-9.6	-12.2
CalVal-RM	0.4	0.5	-0.1	0.1
HEA-RM	-0.5	-0.7	-0.1	0.5
KEA-PR*	0.1	-0.6	-0.2	0.4
SMX-PR	2.1	1.6	1.2	1.3

\* Results are given only for Supertyphoon Thelma.

somewhat misleading. As described in the Appendix, this algorithm utilizes relationships derived from a series of 25 cloud hydrometeor profiles. These cloud profiles give rise to a complex mixture of radiative properties (vertically dependent absorption, emission, scattering processes), all of which have varied responses to the presence of precipitation with varying degrees of nonlinearity. Interpretation of the response to deconvolution is complicated by the averaging process, since a number of the 25 reference profiles will be involved in a retrieval within a single SSM/I scene, each of which has its own unique sensitivity properties vis à vis the deconvolution effect. Nevertheless, it is clear that this type of algorithm is quite sensitive to simultaneous changes in the low-frequency brightness temperatures resulting from the deconvolution process. The implication is that a perturbative inversion procedure can profit from improvements to the spatial resolution of the input data, much more so than the prior algorithms, which are all cast in the form of fixed regression-type relationships, regardless of whether they are physically or empirically derived. Although the overall impact of deconvolution on the time-space-integrated results does not lead to meaningful biases in the KEA algorithm, it is possible that the instantaneous rain rates could be improved by increasing the spatial resolution of the brightness temperature data.

It can be seen from the rain-rate map in Fig. 2b that the KEA-PR rainfall pattern tends to closely follow the 85-GHz brightness temperature field, which is dominated by a strong scattering signal. This accounts for the algorithm's relative insensitivity to stratiform rain and lower overall domain-averaged rain rates seen in Figs. 3a,b, such as exhibited by the SEA-RM method, but for entirely different reasons. Since the relative weight of the high-frequency channel can be controlled in a newer version of the algorithm stemming from its ability to simultaneously incorporate vertically dependent emission and scattering effects (C. Kummerow 1991, personal communication), the oversensitivity to 85 GHz in the Thelma result presented here does not represent an algorithm shortcoming.

The final algorithm (SMX-PR) is also a profile algorithm, which uses six of the seven SSM/I channels. Similar to the other multispectral algorithms, Table 4 indicates this algorithm is mostly insensitive to deconvolution in the time-space averages, regardless of rain-rate cutoff. However, the time mean differences indicate a positive bias of approximately 2% (refer to Table 6). Similar to the SM-RM, CalVal-RM, and HEA-RM algorithms, this algorithm detects the lighter stratiform rain rates. As seen in Figs. 3a,b, its domain-average rain rates are slightly lower than those given by SM-RM and HEA-RM and exhibit the same basic peak structure as SM-RM (with the exception that the domain averages for the three upper cutoffs at the seventh overpass, following the peak at the sixth overpass, do not fall off).

It is also evident from Table 5 that the domain-averaged percentage differences are larger than found with the CalVal-RM and HEA-RM algorithms, albeit only about half the magnitude of the KEA-PR algorithm. By the same token, pixel-level rain-rate differences can exceed  $13 \text{ mm h}^{-1}$ . As with the KEA-PR algorithm, it is also difficult to provide a simple interpretation of the sensitivity to deconvolution. This is because each pixel situation leads to a somewhat unique response in terms nonlinearly related to how the initial-guess and optimization procedures of the algorithm are implemented. By the same token, as with KEA-PR, it is fair to say that although meaningful biases between raw and deconvolved retrievals do not appear in time-space averages, instantaneous rain rates are quite sensitive to deconvolution. Since this is also a perturbative inversion algorithm, it is possible that the algorithm results improve as the resolution of the input data improves.

As a means of graphically demonstrating deconvolution impact on the six algorithms at the pixel scale, a transect through Supertyphoon Thelma at the 2131 UTC overpass has been examined in detail. The black straight line running through the storm core in Fig. 1 indicates the transect path. Figure 5 shows the 19-, 37-, and 85-GHz brightness temperatures associated with the transect, including both the nondeconvolved and deconvolved cases for the lower two frequencies. It is quite easy to see that the basic effect of deconvolution of the brightness temperatures is to sharpen the peaks and valleys within the gradient regions. The algorithm results are given in Fig. 5b. The left panels of this figure show the rain-rate estimates for the nondeconvolved cases; the right panels show the retrieved rain-rate differences with respect to the deconvolved cases. It is evident that for this particular transect the SEA-RM and KEA-PR algorithms exhibit the greatest sensitivity, whereas the CalVal-RM, HEA-RM, and SMX-PR algorithms exhibit the least sensitivity. However, none of the difference transects obtained from these five algorithms indicates preferential bias. This is not the case for the single-frequency emission-based SM-RM algorithm, which exhibits moderate sensitivity but in a purely biased fashion. Most importantly, all of the behavior seen in the various difference transects is consistent with the analysis discussed above.

#### *b. Analysis of additional cyclone cases*

Five of the six algorithms were also applied to six additional tropical cyclone cases identified in Table 1 (KEA-PR results are available only for Thelma because of logistic considerations with Dr. Kummerow). Figure 6 illustrates 85-GHz V-pol images of selected overpasses for each of these storms. The compilation of the time means of domain-averaged percentage differences between raw and deconvolved calculations for each of the cases is presented in Table 4, with extreme values



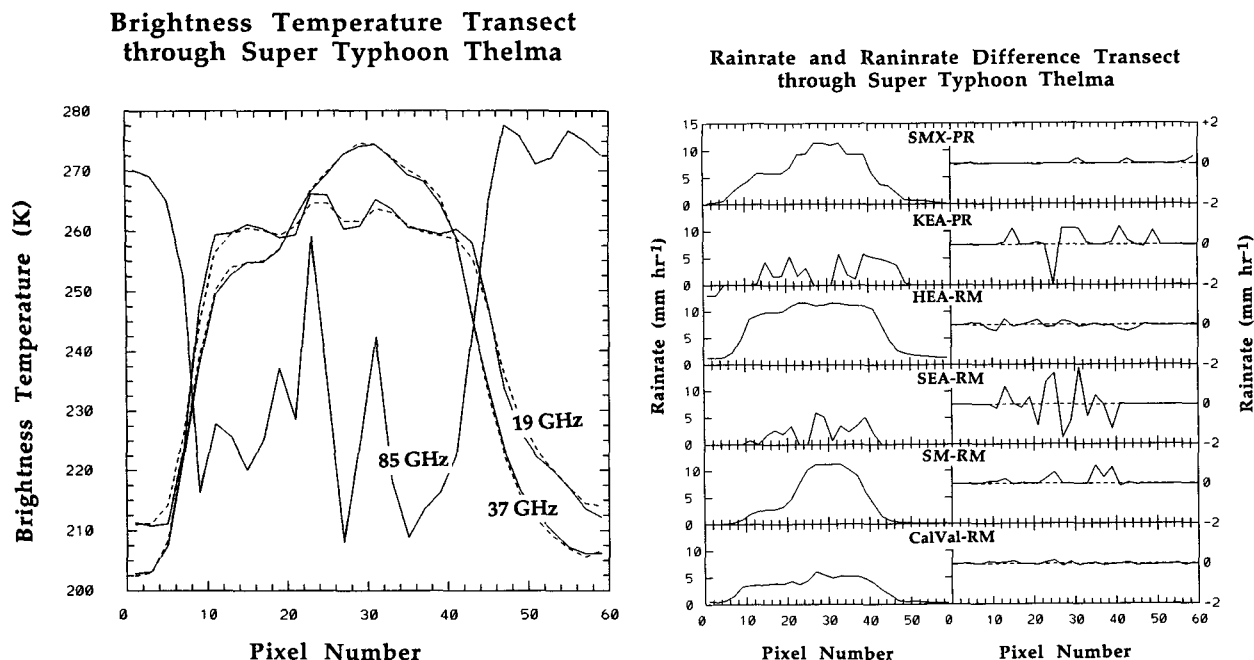


FIG. 5. (a) Brightness temperature transect through Supertyphoon Thelma (see Fig. 1). At the 19- and 37-GHz frequencies, the dashed lines represent nondeconvolved brightness temperatures, whereas the solid lines represent the deconvolved brightness temperatures. (b) Left panel shows rain-rate transects through Thelma based on the nondeconvolved brightness temperatures used as input to the six retrieval algorithms. Right panel shows the rain-rate difference transects obtained by subtracting nondeconvolved solutions from deconvolved solutions.

of the domain-averaged percentage differences summarized in Table 5. Finally, grand averaged differences over all storms for each of the algorithms are given in Table 6.

The basic response of each algorithm found for Supertyphoon Thelma, in terms of relative rain-rate magnitude, sensitivity to stratiform rain, and sensitivity to deconvolution, are duplicated for the other storm cases. Table 4 indicates that the time-space-integrated rain rates from the SM-RM emission-type algorithm consistently increase when deconvolution is applied for every storm case; Table 6 indicates that when lighter rain rates are considered, spatial enhancement produces a grand-averaged increase of 5.2%. These tables also indicate that negative biases are consistently introduced into the SEA-RM algorithm by the deconvolution technique because it is a channel difference method, sensitive to the noise properties of the respective channels. Since the coefficients developed for the 37-GHz PCT by Spencer et al. (1989) were based on raw measurements, they are not consistent with the deconvolved measurements. This is because the noise properties introduced into the spatially enhanced measurements in conjunction with the distinct noise properties of the V-pol and H-pol channel gain functions have been altered.

It is also evident from Tables 4 and 6 that the time-space-averaged rain rates of the CalVal-RM, HEA-RM, KEA-PR, and SMX-PR algorithms are basically in-

sensitive to the deconvolution process. Although these algorithms are radically different in design and philosophy (which leads to marked differences in their rain patterns and domain-averaged rain rates, as well as the domain-averaged percentage differences and pixel-level rain-rate differences at individual overpass times), they share a common trait in that they are all multispectral algorithms (using 5, 4, 7, and 6 channels, respectively). Therefore, although some of the algorithms produce significant rain-rate changes on a pixel-by-pixel basis after the application of the spatial deconvolution scheme, changes that may be considered as improvements over the instantaneous retrievals, these changes are of a random nature and do not induce consistent biases in the time-space averages. In that sense, these algorithms may represent a basic improvement over single-channel algorithms.

## 7. Summary and conclusions

The effect of spatial deconvolution on lower-frequency SSM/I channels has been examined in terms of its impact on rain rates derived from six different precipitation retrieval algorithms, which in effect has revealed how each algorithm is impacted by the problem of nonhomogeneous beam filling. In conducting this study, we have also illustrated some of the relative differences in how individual retrieval algorithms perform with the same datasets.

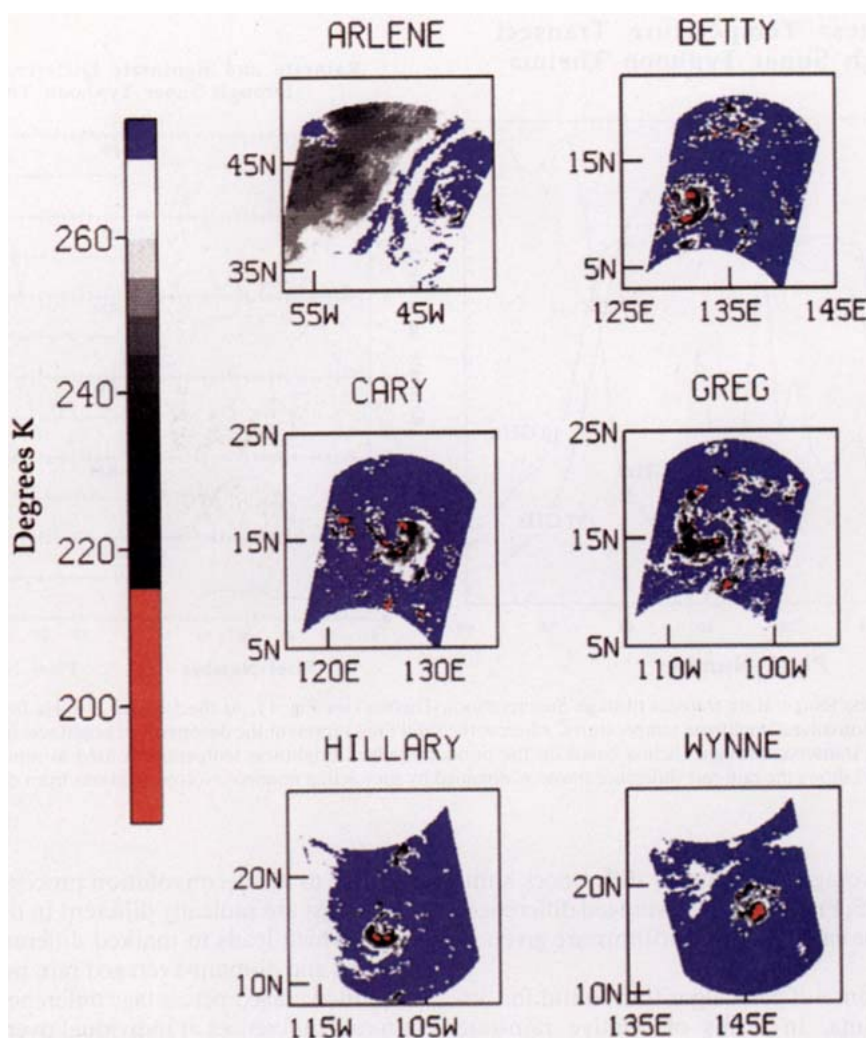


FIG. 6. Microwave images at 85 GHz (V-pol) of 1987 season tropical cyclones Arlene (2156 UTC 22 August), Betty (0916 UTC 10 August), Cary (0955 UTC 15 August), Greg (0118 UTC 30 July), Hillary (1311 UTC 4 August) and Wynne (2021 UTC 5 July). See Table 2 for further descriptions of storms.

The single-frequency SM-RM emission algorithm is simple to use and responds well to storm intensity; however, it is vulnerable to incomplete beam filling. Rainfall from this type of algorithm will be inherently underestimated due to the nonlinear properties of the brightness temperature–rain rate relationship. The single-frequency SEA-RM scattering algorithm is also simple to use and also responds well to storm intensity. However, since it was modeled in terms of the scattering effect of large water drops and ice particles on depolarization, the algorithm is not sensitive to warm stratiform rain. Furthermore, the independent treatment of the different polarized channels in the deconvolution scheme introduces a bias in polarized brightness temperature difference related to engineering-level differences in the noise properties of each channel's gain functions. In turn, this leads to negative rain-rate

biases. This and any other algorithm that relies on polarized brightness temperature differences are susceptible to cross-channel biases if they do not account for the fact that noise properties will be altered during a deconvolution process. The CalVal-RM algorithm, developed for operational DOD applications, produces the lowest domain-averaged rain rates but does not exhibit meaningful bias between raw and deconvolved rain-rate calculations averaged in time and space. The dual frequency, four-channel HEA-RM algorithm responds well to storm intensity, and while its threshold to distinguish between no rain and light rain is inadequate for SSM/I purposes (this algorithm was designed for SMMR applications whose low-frequency channel is 18 GHz instead of 19.35 GHz as used on SSM/I), it does not indicate a bias in its averaged rain rates due to nonhomogeneous beam filling.

The multiple-frequency KEA-PR and SMX-PR profile algorithms are based on strong physics and are designed to respond to the vertical structures in different types of precipitating clouds. Neither of these two algorithms exhibit meaningful biases between the raw and deconvolved averaged rain rates at the time-space-averaged scale, although significant differences are found at the pixel scale. Because both these algorithms utilize a variety of different cloud profiles as initial guess information, each of which has its own unique impact on deconvolution sensitivity, it is somewhat difficult to quantify the general nonlinear transform relationships associated with the profile algorithms. Both algorithms respond well to storm intensification, although they produce significantly different rain-rate maps. The former algorithm employs all four SSM/I frequencies, although for the case examined here, the rain-rate patterns tend to mimic the behavior of the 85-GHz channel, explaining its lack of sensitivity to stratiform rain. (This is not a fixed property of the algorithm, as the relative weight of each frequency on the retrievals can be altered.) The SMX-PR algorithm is a three-frequency algorithm that detects both convective and stratiform rain and tends to produce continuity in the domain averages as the rain-rate cutoff is increased. This algorithm exhibits the same basic response to deconvolution as the KEA-PR algorithm, although the domain-averaged rain-rate differences for individual overpasses are not as large.

While the effect of deconvolution on each of the algorithms is quite different at the pixel scale, the multispectral algorithms appear to be mostly impervious to bias in the time-space averages. Therefore, spatial deconvolution would not be expected to impact heavily averaged rainfall datasets, such as those required for climate studies. By the same token, the retrieval of instantaneous rain rates generally improves as the spatial resolution increases, particularly in high-gradient situations such as storm cores and along convection lines where rain rates tend to be large and relatively important to volume-integrated rainfall. Thus, spatial deconvolution should be viewed as a desirable feature of a retrieval algorithm if instantaneous rain rates are required. The two profile algorithms tested in this study may profit most of spatial resolution enhancement because they utilize perturbative inversion techniques responsive to detailed brightness temperature structures.

A further advantage of the spatially enhanced data is that smaller-scale features can be better identified and visualized as shown in the study of Farrar and Smith (1992). This alone can make positive contributions to the analysis and forecasting of precipitating storms. Therefore, it is reasonable to conclude that microwave radiometers designed with rain retrieval in mind should continue to provide as much footprint overlap as possible under the engineering constraints, until such time that technology can achieve across-the-board high resolution at all frequencies.

*Acknowledgments.* The authors sincerely appreciate the assistance and cooperation of Barry Hinton, Christian Kummerow, and Roy Spencer in making the calculations needed for this study. Jim Hollinger, Gene Poe, and Richard Savage kindly provided SSM/I technical information and some very helpful discussions. The authors also wish to thank Jim Merritt for his capable assistance in computational support. This research has been supported by NASA Grants NAGW-991 and NAG5-1602. A portion of the computing resources has been provided by the Supercomputer Computations Research Institute at The Florida State University under DOE Contract FC058ER250000.

## APPENDIX

### Description of Six Precipitation Retrieval Algorithms

The following presents brief descriptions of the six algorithms used in conducting this study. Table 3 provides the naming convention and the relevant references.

#### *a. SM-RM*

This algorithm was developed from radiative transfer calculations based on the simulation of a precipitating cloud (Smith and Mugnai 1988). A highly detailed microwave radiative transfer model, developed by Mugnai and Smith (1988), was coupled to an explicit microphysical model of a time-dependent cumulus cloud. The coupled model was used to associate rain rates with top of atmosphere (TOA) brightness temperatures at various microwave frequencies as the cloud developed in time and the thickness of the rain layer increased. Knowledge of rain rates as a function of the microphysical and dynamical aspects of a precipitating cloud were incorporated within the model framework, so that a most probable rain rate could be associated with the sequence of cloud development times. Hence, a most probable rain rate related to a given cloud development time and rain layer thickness could be expressed as a function of TOA brightness temperature. For the calculations made in this study, the 19-GHz brightness temperature-rain rate relationship was used.

The brightness temperature-rain rate function for 19 GHz is presented in Fig. 4. The most notable features of this diagram are its strong nonlinear properties and its double-valued behavior. As the cloud develops, upwelling radiation from the lower rain layers is mostly absorbed, with the rain signal from the middle and upper layers growing rapidly, leading to higher brightness temperatures at the TOA. As the cloud continues to develop, its rain optical depth reaches a critical limit (saturation), in which the predominant emission sources of radiation reaching the TOA are only at or above the top of the rain layer. Beyond that point, continued development leads to a situation in which backscattering by larger rain drops in the middle and

upper cloud layers begins to depress the limited emission signals, in effect masking radiation from the rain layer top. Hence, as the rain rate increases beyond the saturation limit (also referred to as the blackbody limit), the function between rain rate and TOA brightness temperature becomes double valued.

### b. SEA-RM

This single-frequency (37 GHz) algorithm is based on the depolarization of microwave brightness temperatures due to scattering by hydrometeors, which was shown by Spencer et al. (1989) to be dominated by the effects of ice. As these hydrometeors (especially ice) scatter upwelling radiation signals out of the path, the values of the resulting TOA temperatures are reduced. It was then shown that the polarization diversity of the SSM/I measurements allows low but highly polarized brightness temperatures arising from the ocean surface to be distinguished from low but depolarized brightness temperatures emanating from the precipitating clouds.

The polarization information was formulated in terms of a polarization-corrected temperature (PCT) defined as

$$\text{PCT} = \frac{\beta T_{Bh} - T_{Bv}}{\beta - 1}, \quad (\text{A1})$$

where

$$\beta = \frac{T_{Bvc} - T_{Bvo}}{T_{Bhc} - T_{Bho}}. \quad (\text{A2})$$

Here  $T_{Bvc}$  and  $T_{Bhc}$  refer to the respective polarized  $T_B$ 's over a cloud-free ocean, while  $T_{Bvo}$  and  $T_{Bho}$  represent  $T_B$ 's over an idealized ocean lacking an overlying atmosphere. Each of these parameters was derived from model calculations for a standard tropical atmosphere over the ocean at the SSM/I viewing angle of  $53^\circ$ . As actual SSM/I measurements differed significantly from model expectations, an empirically modified value of  $\beta$  was derived. When this value was applied to the 37-GHz measurements, the expression for the polarization-corrected temperature at 37 GHz reduced to the following:

$$\text{PCT}_{37} = 2.1T_B(37V) - 1.1T_B(37H). \quad (\text{A3})$$

A threshold value of the PCT was then found such that any value larger than the threshold would be considered too highly polarized to represent significant precipitation. As this method relies on effects due to ice and large hydrometeors, it fails to identify shallow, light precipitation. Rain rates (RR) are inferred from the threshold PCT (270 K) and the 37-GHz polarization-corrected temperatures with a linear equation:

$$\text{RR} (\text{mm h}^{-1}) = 270 - \text{PCT}_{37}. \quad (\text{A4})$$

### c. CalVal-RM

This statistical algorithm (CalVal 1991) was derived from a regression using an exponential function of SSM/I-measured brightness temperatures against radar-derived "ground truth" rain-rate data. The general form of the regression function is

$$\text{RR} (\text{mm h}^{-1}) = \exp(a_0 + \sum_{i=1}^N a_i T_{B_i}) - c, \quad (\text{A5})$$

where  $N$  is the total number of channels (seven for SSM/I);  $T_{B_i}$  is the brightness temperature for each respective channel; and  $a_0$ ,  $a_i$ , and  $c$  are the regression coefficients. Ground-truth rain rates over the ocean were obtained from two tropical radar sites (Darwin, Australia, and Kwajalein, Marshall Islands). A total of 1361 collocated SSM/I and radar observations were selected for the training dataset, where only 241 of the radar-derived rain rates had values greater than  $0.5 \text{ mm h}^{-1}$ . As noted in CalVal (1991, 11–31), this algorithm underestimates rain rates greater than  $5 \text{ mm h}^{-1}$ . This is presumably related to an insufficient number of high radar-derived rain rates in the training dataset (W. Olson 1991, personnel communication).

The regression based on these collocated measurements takes the form

$$\begin{aligned} \text{RR} (\text{mm h}^{-1}) = & \exp(3.06231 - 0.0056036T_{B85V} \\ & + 0.0029478T_{B85H} - 0.0018119T_{B37V} \\ & - 0.00750T_{B22V} + 0.0097550T_{B19V}) - 8.0. \end{aligned} \quad (\text{A6})$$

If a combination of brightness temperature leads to a calculation of rain rate less than 0, then the retrieved value is set to 0. It should be noted in (A6) that only five of the seven channels are retained in the regression because the contributions to additional explained variance by the 37- and 19-GHz H-pol measurements were not found to be significant in the regression calculations.

### d. HEA-RM

This algorithm represents a set of single-channel physical-statistical models developed for the SMMR instrument aboard the *Nimbus-7* satellite. The design of the algorithm and results for Indian Ocean rainfall are given by Hinton et al. (1992); further details can be found in Hinton et al. (1990). A plane-parallel, 120-layer radiative transfer model was used to determine the upwelling brightness temperatures over  $1^\circ \times 1^\circ$  latitude boxes as a function of various model parameters, some of which were prescribed with typical climatological values and others concerning radiative properties obtained from model tests. Sensitivity tests of all these parameters found that variations in non-precipitating cloud water liquid water content (LWC) dominated the variations in the resultant brightness

temperatures. Thus, the presence of nonprecipitating cloud droplets introduced uncertainty in the rain rates, but at the same time could be linked to dynamical processes that produced the precipitation. Therefore, a semiempirical relationship between rainrate and nonprecipitating LWC was introduced in an effort to remove some of the ambiguity in the model-derived brightness temperature–rain rate relationships. The results for each  $1^\circ \times 1^\circ$  box were then integrated with a prescribed statistical distribution to match the field of view of the SMMR instrument, so that an area-averaged rain rate could be calculated from an area-averaged brightness temperature measured at the satellite.

The following equations were then obtained from polynomial regressions of the averaged rain rates against the averaged brightness temperature for each of the four channels:

$$RR_{18V} = \begin{cases} 0, & T_B(18V) \leq 192.283 \\ 0.06295[T_B(18V) - 192.283] \\ + 2.0 \times 10^{-5}[T_B(18V) - 192.283]^3, & T_B(18V) > 192.283, \\ 12, & RR_{18V} > 12 \end{cases} \quad (A7a)$$

$$RR_{18H} = \begin{cases} 0, & T_B(18H) \leq 133.763 \\ 0.038162[T_B(18H) - 133.763] \\ + 3.87 \times 10^{-6}[T_B(18H) - 133.763]^3, & T_B(18H) > 133.763, \\ 12, & RR_{18H} > 12 \end{cases} \quad (A7b)$$

$$RR_{37V} = \begin{cases} 0, & T_B(37V) \leq 213.38 \\ -5.0199 + 0.02333T_B(37V) + 0.6272 \\ \times \exp\{[T_B(37V) - 258]/3.3655\}, & T_B(37V) > 213.38, \\ 12, & RR_{37V} > 12 \end{cases} \quad (A7c)$$

$$RR_{37H} = \begin{cases} 0, & T_B(37H) \leq 159.42 \\ -1.3973 + 0.008942T_B(37H) + 3.8394 \\ \times \exp\{[T_B(37H) - 258]/11.0530\}, & T_B(37H) > 159.42 \\ 12, & RR_{37H} > 12. \end{cases} \quad (A7d)$$

These four algorithms were weighted by the inverses of their rain-rate variances, which were obtained by multiplying the known channel-dependent brightness temperature variances by the partial derivatives of rain rate with brightness temperature determined experimentally from model studies of each channel. As the measurement errors are assumed to be random, then the individual weights are proportional to the inverse square of the derivative of RR with respect to  $T_B$  times the error variance for each channel. The weights for

each channel were then expressed as a function of the respective rain rate, as follows:

$$\begin{aligned} W_{18V} &= 0.175[1 - \exp(-1.53RR_{18V})] \\ &\times \exp(-0.0717RR_{18V}) \\ W_{18H} &= 0.516[1 - \exp(-1.39RR_{18H})] \\ &\times \exp(-0.0698RR_{18H}) \\ W_{37V} &= 0.004 + 0.125 \exp(-RR_{37V}) \\ W_{37H} &= 0.019 + 0.776 \exp(-RR_{37H}), \end{aligned} \quad (A8)$$

where the right-hand sides are statistical fits to the inverse expressions. The final rain rate is then found by applying the weights of (A8) to each respective single-channel rain rate found from (A7), summing, and then dividing by the sum of the weights. As previously noted, the regression equations were developed for the SMMR frequencies of 18 and 37 GHz but applied to SSM/I data measurements at 19.35 and 37 GHz.

#### e. KEA-PR

This multiple-frequency algorithm employs relationships between rain rates and brightness temperatures, derived from a set of 25 cloud radiative models based on microphysical profiles derived from aircraft radar measurements. The algorithm has been described by Kummerow et al. (1991); Kummerow et al. (1989) contains useful background information. Each model consists of five vertical layers and specifies a distinct vertical cloud structure in terms of cloud liquid water and rain rate. Ten of the models are defined as “convective,” indicating the presence of significant quantities of liquid and frozen hydrometeors above the freezing level. Ten models are identified as “stratiform,” indicating the absence of liquid hydrometeors above the freezing level. The final five models are defined as “anvil clouds,” characterized by ice aloft but no significant precipitation at the surface, such as those clouds often observed in downwind or “blowoff” regions of convective systems. The retrieval scheme determines which of these models best represents the observed meteorological conditions as outlined by the following procedure.

First, various quantities within each cloud model are varied randomly to produce a large set of possible clouds. Multiple linear regression techniques are applied to the upwelling brightness temperatures produced by a given model to obtain regression coefficients relating the rainfall rate (RR) to a linear combination of the observed brightness temperatures. This is expressed by

$$RR \text{ (mm h}^{-1}\text{)} = a_0 + \sum_{i=1}^N a_i T_{B_i}, \quad (A9)$$

where  $N$  is the total number of channels (seven for SSM/I),  $T_{B_i}$  are the brightness temperatures for the respective channels, and  $a_0$  and  $a_i$  are the regression coefficients. By requiring consistency between the observed  $T_B$ 's and those calculated from the models, the retrieval scheme can determine which of the models best represents the observed microphysical conditions.

#### f. SMX-PR

This multiple-frequency profile algorithm is based on a multiconstituent inversion scheme. The design and technical features of the algorithm are described in Smith et al. (1992a), Smith et al. (1992b), and Smith et al. (1994), Mugnai et al. (1993), and Xiang et al. (1992). During the inversion process, initial-guess vertical profiles of liquid and frozen hydrometeor distributions are adjusted in a forward radiative transfer model until modeled brightness temperatures are brought into agreement with measurements at three frequencies (19, 37, and 85 GHz). The solution liquid water and ice water content profiles, resolved to many levels (greater than 30), are then used to produce vertically dependent liquid and frozen rain rates and latent heat profiles. The initial-guess profiles, used as input to the forward radiative transfer model, are obtained from a mesoscale cloud model (see Tripoli 1992) representing a large ensemble of microphysical situations. The radiative transfer model is a polarized Sobolev two-stream solution of the azimuthally independent radiative transfer equation, designed for applications in the microwave spectrum (see Xiang 1989).

The combinations of microphysical profiles and modeled upwelling brightness temperatures are assembled into a database, which is used to provide first-guess information for each pixel-level measurement. As each brightness temperature measurement set is input, an initial-guess profile domain is identified that brackets the measurement using a scheme involving opposite-signed differences of the measured and modeled brightness temperatures. Linear combinations of these start-up profiles are then perturbed until the differences between the modeled and measured brightness temperatures at the individual frequencies are minimized. The perturbation process is guided by an explicit optimization scheme designed to avoid nonuniqueness problems once an initial guess domain is identified. The algorithm generates vertical profiles of liquid-ice water contents for precipitating rain and ice, as well as suspended cloud droplets and ice crystals. These profiles are then used to derive vertically dependent rain rates (including surface rain rates) from gravity fallout equations as given in Mugnai et al. (1993). This allows the calculation of the water-ice mass flux profiles whose vertical derivatives are proportional to latent heating along a vertical column.

#### REFERENCES

- Adler, R. F., A. J. Negri, P. R. Keehn, and I. M. Hakkarinen, 1993: Estimation of monthly rainfall over Japan and surrounding waters from a combination of low-orbit microwave and geosynchronous IR data. *J. Appl. Meteor.*, **32**, 335–356.

- Arkin, P. A., and B. N. Meisner, 1987: The relationship between large-scale convective rainfall and cold cloud over the western hemisphere during 1982–84. *Mon. Wea. Rev.*, **115**, 51–74.
- Backus, G., and F. Gilbert, 1970: Uniqueness in the inversion of inaccurate gross earth data. *Philos. Trans. Roy. Soc. London*, **A266**, 123–192.
- CalVal, 1989: DMSP Special Sensor Microwave/Imager Calibration/Validation. Final Report—Vol. I. Naval Research Laboratory, Washington, D.C., 176 pp.
- , 1991: DMSP Special Sensor Microwave/Imager Calibration/Validation. Final Report—Vol II. Naval Research Laboratory, Washington, D.C., 277 pp.
- Case, R. A., and H. P. Gerrish, 1988: Annual summary: Atlantic hurricane season of 1987. *Mon. Wea. Rev.*, **116**, 939–949.
- Chiu, L. S., G. R. North, D. A. Short, and A. McConnell, 1990: Rain estimation from satellites: Effect of finite field of view. *J. Geophys. Res.*, **95**, 2177–2185.
- Claassen, J. P., and A. K. Fung, 1974: The recovery of polarized apparent temperature distributions of flat scenes from antenna temperature measurements. *IEEE Trans. Antennas Propag.*, **AP-22**, 433–442.
- Cross, R. L., 1988: Annual summary: Eastern North Pacific tropical cyclones of 1987. *Mon. Wea. Rev.*, **116**, 2106–2117.
- Farrar, M. R., and E. A. Smith, 1992: Spatial resolution enhancement of terrestrial features using deconvolved SSM/I microwave brightness temperatures. *IEEE Trans. Geosci. Remote Sens.*, **30**, 349–355.
- Hinton, B. B., D. W. Martin, B. Auvine, and W. S. Olson, 1990: Use of microwave satellite data to study variations in rainfall over the Indian Ocean. Final Report on Grant NAGW-920, 58 pp. [Available from Space Science and Engineering Center, University of Wisconsin, Madison, WI 53706.]
- , W. S. Olson, D. W. Martin, and B. Auvine, 1992: A passive microwave algorithm for tropical oceanic rainfall. *J. Appl. Meteor.*, **31**, 1379–1395.
- Hoffman, C. W., V. G. Patterson, and D. J. McMorro, 1987: 1987 tropical cyclone report. Joint Typhoon Warning Center, Guam, 213 pp.
- Hollinger, J. P., J. L. Pierce, and G. A. Poe, 1990: SSM/I instrument evaluation. *IEEE Trans. Geosci. Remote Sens.*, **GE-28**, 800–810.
- Holmes, J. J., C. A. Balanis, and W. M. Truman, 1975: Application of Fourier transforms for microwave radiometric inversions. *IEEE Trans. Antennas Propag.*, **AP-23**, 797–806.
- Kummerow, C., R. A. Mack, and I. M. Hakkarinen, 1989: A self-consistency approach to improve microwave rainfall estimates from space. *J. Appl. Meteor.*, **28**, 869–884.
- , I. M. Hakkarinen, H. F. Pierce, and J. A. Weinman, 1991: Determination of precipitation profiles from airborne passive microwave radiometric measurements. *J. Atmos. Oceanic Technol.*, **8**, 148–158.
- Lewis, B. M., and D. P. Jorgensen, 1978: Study of the dissipation of Hurricane Gertrude (1974). *Mon. Wea. Rev.*, **106**, 1288–1306.
- Mugnai, A., and E. A. Smith, 1988: Radiative transfer to space through a precipitating cloud at multiple microwave frequencies. Part I: Model description. *J. Appl. Meteor.*, **27**, 1055–1073.
- , H. J. Cooper, E. A. Smith, and G. J. Tripoli, 1990: Simulation of microwave brightness temperatures of an evolving hailstorm at SSM/I frequencies. *Bull. Amer. Meteor. Soc.*, **71**, 2–13.
- , E. A. Smith, and G. J. Tripoli, 1993: Foundations for physical-statistical precipitation retrieval from passive microwave satellite measurements. Part II: Emission source and generalized weighting function properties of a time dependent cloud-radiation model. *J. Appl. Meteor.*, **32**, 17–19.
- Olson, W. S., 1989: Physical retrieval of rainfall rates over the ocean by multispectral microwave radiometry: Application to tropical cyclones. *J. Geophys. Res.*, **94**, 2267–2280.
- , C. Yeh, J. A. Weinman, and R. T. Chin, 1986: Resolution enhancement of multichannel microwave imagery from the



- Nimbus-7 SMMR for maritime rainfall analysis. J. Atmos. Oceanic Technol.*, **3**, 422–432.
- Poe, G., 1990: Optimum interpolation of imaging microwave radiometer data. *IEEE Trans. Geosci. Remote Sens.*, **GE-28**, 800–810.
- Robinson, W. D., C. Kummerow, and W. S. Olson, 1992: A technique for enhancing and matching the resolution of microwave measurements from the SSM/I instrument. *IEEE Trans. Geosci. Remote Sens.*, **GE-30**, 419–429.
- Rodgers, E. B., and R. F. Adler, 1981: Tropical cyclone rainfall characteristics as determined from a satellite passive microwave radiometer. *Mon. Wea. Rev.*, **109**, 506–521.
- Shin, K., P. E. Riba, and G. R. North, 1990: Estimation of area-averaged rainfall over tropical oceans from microwave radiometry: A single channel approach. *J. Appl. Meteor.*, **29**, 1031–1042.
- Short, D. A., and G. R. North, 1990: The beam filling error in the *Nimbus 5* Electrically Scanning Microwave Radiometer observations of Global Atlantic Tropical Experiment rainfall. *J. Geophys. Res.*, **95**, 2187–2193.
- Smith, E. A., and S. Q. Kidder, 1978: A multispectral satellite approach to rainfall estimates. Tech. Rep., Department of Atmospheric Sciences, Colorado State University, Ft. Collins, CO, 49 pp.
- , and A. Mugnai, 1988: Radiative transfer to space through a precipitating cloud at multiple microwave frequencies. Part II: Results and analysis. *J. Appl. Meteor.*, **27**, 1074–1091.
- , and —, H. J. Cooper, G. J. Tripoli, and X. Xiang, 1992a: Foundations for physical-statistical precipitation retrieval from passive microwave satellite measurements. Part I: Brightness temperature properties of a time dependent cloud-radiation model. *J. Appl. Meteor.*, **31**, 506–531.
- , X. Xiang, A. Mugnai, and G. J. Tripoli, 1992b: A cloud-radiation model algorithm for spaceborne precipitation retrieval. *Extended Abstracts, Int. TRMM Workshop on the Processing and Utilization of the Rainfall Data Measured from Space*, Tokyo, Japan, Communications Research Laboratory, 273–283.
- , —, —, R. Hood, and R. W. Spencer, 1994: Behavior of an inversion-based precipitation retrieval algorithm with high resolution AMPR measurements including a low frequency 10.7 GHz channel. *J. Atmos. Oceanic Technol.*, **11**, in press.
- Spencer, R. W., 1986: A satellite passive 37-GHz scattering-based method for measuring oceanic rain rates. *J. Climate Appl. Meteor.*, **25**, 754–766.
- , H. M. Goodman, and R. Hood, 1989: Precipitation retrieval over land and ocean with the SSM/I: Identification and characteristics of the scattering signal. *J. Atmos. Oceanic Technol.*, **6**, 254–273.
- Stogryn, A., 1978: Estimates of brightness temperatures from scanning radiometer data. *IEEE Trans. Antennas Prop.*, **AP-26**, 720–726.
- Tripoli, G. J., 1992: A nonhydrostatic model designed to simulate scale interaction. *Mon. Wea. Rev.*, **120**, 1342–1359.
- Wilheit, T. T., A. T. C. Chang, M. S. V. Rao, E. B. Rodgers, and J. S. Theon, 1977: A satellite technique for quantitatively mapping rainfall rates over the ocean. *J. Appl. Meteor.*, **16**, 551–560.
- , —, and L. S. Chiu, 1991: Retrieval of monthly rainfall indices from microwave radiometric measurements using probability distribution functions. *J. Atmos. Oceanic Technol.*, **8**, 118–136.
- Xiang, X., 1989: The delta-Sobolev approach for modeling solar spectral irradiance and radiance. Ph.D. dissertation, Georgia Institute of Technology, 178 pp.
- , E. A. Smith, and G. J. Tripoli, 1992: A cloud and radiation model-based algorithm for rainfall retrieval from SSM/I multispectral microwave measurements. Preprints, *Sixth Conf. on Satellite Meteorology and Oceanography*, Atlanta, GA, Amer. Meteor. Soc., 286–289.